

PCB-RandNet: Rethinking Random Sampling for LIDAR Semantic Segmentation in Autonomous Driving Scene

Huixian Cheng, Xian-Feng Han, Hang Jiang, Dehong He, Guoqiang Xiao

College of Computer and Information Science, Southwest University, Chongqing, China
 chenghuixian@email.swu.edu.cn {xianfenghan, gqxiao}@swu.edu.cn

Abstract

Fast and efficient semantic segmentation of large-scale LiDAR point clouds is a fundamental problem in autonomous driving. To achieve this goal, the existing point-based methods mainly choose to adopt Random Sampling strategy to process large-scale point clouds. However, our quantitative and qualitative studies have found that Random Sampling may be less suitable for the autonomous driving scenario, since the LiDAR points follow an uneven or even long-tailed distribution across the space, which prevents the model from capturing sufficient information from points in different distance ranges and reduces the model's learning capability. To alleviate this problem, we propose a new **Polar Cylinder Balanced Random Sampling** method that enables the downsampled point clouds to maintain a more balanced distribution and improve the segmentation performance under different spatial distributions. In addition, a sampling consistency loss is introduced to further improve the segmentation performance and reduce the model's variance under different sampling methods. Extensive experiments confirm that our approach produces excellent performance on both SemanticKITTI and SemanticPOSS benchmarks, achieving a 2.8% and 4.0% improvement, respectively.

1 Introduction

Recently, with the rapid development of 3D computer vision, great advances have been achieved in autonomous driving [Geiger, Lenz, and Urtasun 2012, Feng et al. 2020], which highly depends on accurate, robust, reliable, and real-time 3D semantic perception and understanding of surroundings. For all sensors equipped in autonomous vehicles, LiDAR sensors play an important role, since (1) LiDAR cannot be affected by light changing, and it is more suitable for different environments. (2) 3D point cloud data generated by LiDAR is becoming increasingly available, and can provide much richer spatial and geometric information. Therefore, LiDAR-based semantic segmentation task, producing point-wise semantic labels, has been attracting more and more attention. Currently, the existing approaches can be summarized into three categories: Voxel-based [Choy, Gwak, and Savarese 2019], Projection-based [Wu et al. 2018, Milioto et al. 2019], and Point-based methods [Qi et al. 2017a,b].

Copyright © 2023, Association for the Advancement of Artificial Intelligence (www.aaai.org). All rights reserved.

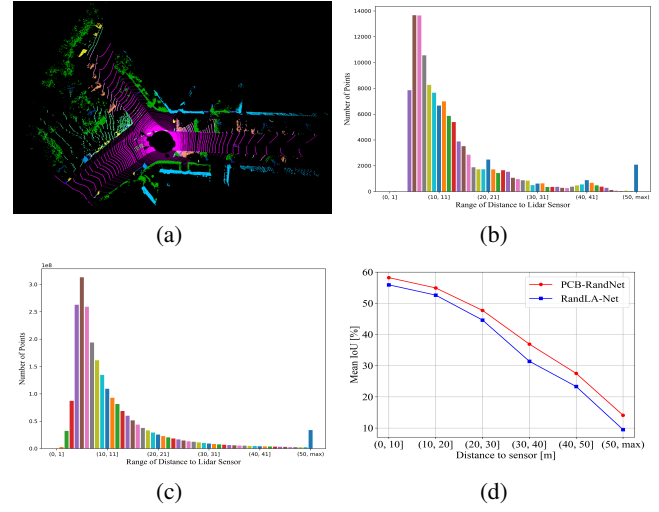


Figure 1: (a): Visualization of one frame of LiDAR scan on the SemanticKITTI dataset. (b): Visualization of the corresponding point cloud scan distance distribution. (c): Visualization of the distance distribution of all training data. (d): Segmentation performance of the baseline method and our method at different distances.

Where voxel-based methods attempt to translate 3D point cloud into structured voxel representation, which is then fed into 3D convolutional networks for feature learning. Although these methods achieve state-of-the-art performance, larger voxel resolutions readily lead to higher computation cost and model complexity, which limits their efficiency performance. Projection-based approaches choose to project 3D point cloud into representations in 2D space (e.g., range view or bird's-eye view), and utilize 2D convolution operations to process them with a high inference speed. However, such methods have not fully taken advantage of 3D geometric information due to the introduction of information loss during projection.

Point-based methods can directly deal with raw disordered, unstructured 3D point clouds without any information loss. Although these methods have produced encouraging results in terms of object classification and part segmen-

tation, most are only suitable for small-scale point clouds or indoor scenes, and cannot be directly extended to large-scale cases. This is mainly because the usage of the farthest point sampling (FPS) operation causes much higher computational complexity and memory consumption [Qi et al. 2017b, Li et al. 2018, Wu, Qi, and Fuxin 2019, Yan et al. 2020]. Specifically, for an input of 10^6 points, FPS requires more than 200 seconds to sample it to 10%. To address this problem, RandLA-Net [Hu et al. 2020] proposes a new efficient and lightweight neural architecture by combining simple **Random Sampling (RS)** and local feature aggregation modules, which achieves high efficiency and state-of-the-art performance on multiple benchmarks.

However, when revisiting the random sampling method used in RandLA-Net for the task of outdoor LiDAR semantic segmentation, we get the following findings. Taking a randomly selected frame (Seq:00 ID:0000) of point cloud data (shown in Figure 1a) from the SemanticKITTI dataset as an example, we quantitatively visualize its density (or the number of points) distribution with respect to distance between points and LiDAR sensor. And it clearly follows a long-tail distribution. That is, the closer the distance to sensor is, the point clouds are much more dense. And they become sparser as the distance increases.

Here is one question: **Is random sampling still applicable to such a specific autonomous driving scenario?** Obviously, the answer is **No**. Because Random Sampling selects M points evenly from the initial N points, where each point has the same probability of being selected [Hu et al. 2020]. However, through qualitative and quantitative analysis, we have found that points at close distances have a high possibility of being retained, while points at medium and long distances tend to be discarded, which results in reduction of model's capability of learning sufficient representation from points in different distance ranges. As shown in Figure 1d, it can be reported that the segmentation performance of the model decreases sharply as the distance to the sensor increases.

To address this problem, we propose a novel sampling method, termed **Polar Cylinder Balanced Random Sampling (PCB-RS)**. Specifically, we first divide the input point cloud into different cylindrical blocks in the polar BEV view, and then perform the balanced random sampling within each block. The downsampled point cloud can maintain a more balanced distribution, which guides the network to sufficiently learn point features at different distances, and improve the segmentation performance within different distance ranges (as shown in Figure 1d). In addition, we present a **Sampling Consistency Loss (SCL)** function to reduce the model variation under different sampling methods.

We evaluate our proposed approach on two large-scale outdoor autonomous driving scenario datasets, namely SemanticKITTI and SemanticPOSS. Experimental results show that our method improves the baseline RandLANet by 2.8mIoU on the SemanticKITTI dataset and by 4mIoU on the SemanticPOSS dataset.

The main contributions of this work can be summarized as follows:

- We propose a novel Polar Cylinder Balanced Random

Sampling method to downsample the point clouds, which contributes to guiding the segmentation model to better learn the point distribution characteristics in autonomous driving scenario.

- We propose a sampling consistency loss function to reduce the model's variance under different sampling approaches.
- Experimental results on SemanticKITTI and SemanticPOSS demonstrate the superior performance of our proposed method.

2 Related work

Voxel-based Methods first discretize point clouds into 3D voxel representations and then predict the semantic labels for these voxels using 3D CNN frameworks. MinkowskiNet [Choy, Gwak, and Savarese 2019] chose to use sparse convolution instead of standard 3D convolution to reduce computation cost. SPVNas [Tang et al. 2020] utilizes neural structure search (NAS) to further improve the performance of the network. JS3C-Net [Yan et al. 2021] proposes an enhanced joint single-scan LiDAR point cloud semantic segmentation method, which uses the shape prior learned from the scene completion network to assist in the semantic segmentation. Cylinder3D [Zhou et al. 2020] uses a cylindrical coordinate system to partition voxels.

Projection-based Methods typically perform spherical projection to convert the input LiDAR point clouds into regular 2D images and employ the existing image segmentation methods to avoid processing the irregular and sparse 3D points. In addition, the usage of 2D CNNs can boosts inference speed.

SqueezeSeg [Wu et al. 2018] is the pioneering work that uses spherical projection to convert irregular LiDAR points into 2D images and performs semantic segmentation using the lightweight models SqueezeNet and Conditional Random Field (CRF). Based on SqueezeSeg, SqueezeSeg V2 [Wu et al. 2019] proposes a contextual aggregation module (CAM) to reduce the impact of missing points in LiDAR point clouds and explores the domain adaptation problem between different datasets. RangeNet++ [Milioto et al. 2019] utilizes the DarkNet backbone as an extractor and proposes an efficient KNN post-processing method to predict the point-wise labels to avoid discretization artifacts. SqueezeSegV3 [Xu et al. 2020] proposes a spatially adaptive convolution (SAC) using different filters depending on the location of the input image.

Instead of spherical projection, PolarNet [Zhang et al. 2020] uses a polar bird's-eye-view representation. By balancing the points in the grid cells under the polar coordinate system, the attention of the segmentation network indirectly coincides with the long-tail distribution of points along the radial axis.

Point-based Methods take unordered points as input and predict point-wise semantic labels. PointNet [Qi et al. 2017a] and PointNet++ [Qi et al. 2017b] are pioneering studies that utilize shared MLPs to learn the point-wise properties, which greatly boosts the development of point-based networks. KPConv [Thomas et al. 2019] develops de-

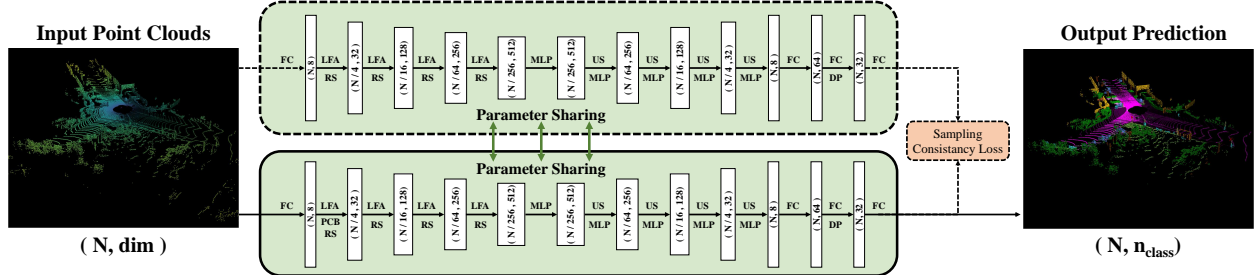


Figure 2: **Overall pipeline of PCB-RandNet.** Our network structure remains the same as RandLA-Net, with **only changes to the first sampling method**. Two different class prediction distributions P_1 and P_2 can be obtained by forwarding the input point cloud twice by models with different sampling methods but shared parameters. Then, the sampling consistency loss between the two class prediction probabilities is calculated and used to supervise the model. (N, D) represents the number of points and feature dimension respectively. RS: Random Sampling, PCB-RS: Polar Cylinder Balanced Random Sampling, FC: Fully Connected layer, LFA: Local Feature Aggregation, MLP: shared Multi-Layer Perceptron, US: Up-sampling, DP: Dropout.

formable convolution, which can use a flexible approach to learn local representations with any number of kernel points. PointASNL [Yan et al. 2020] proposes an adaptive sampling module to efficiently handle point clouds with noise by re-weighting the neighbors around the initial sampling point from the farthest point sampling (FPS). RandLA-Net [Hu et al. 2020] uses random sampling method to significantly improve the efficiency of processing large-scale point clouds and uses local feature aggregation to effectively preserve geometric details and reduce the information loss caused by random operations. BAF-LAC [Shuai, Xu, and Liu 2021] proposes a backward attention fusion encoder-decoder that learns semantic features and a local aggregation classifier that maintains context-awareness of points to extract distinguished semantic features and predict smoother results. BAAF [Qiu, Anwar, and Barnes 2021] obtains more accurate semantic segmentation by using bilateral structures and adaptive fusion methods that take full advantage of the geometric and semantic features of the points.

3 Methodology

3.1 Overview

The overall structure of our PCB-RandNet model is illustrated in Figure 2. We will detailedly describe the Baseline Network, Polar Cylinder Balanced Random Sampling and Sampling Consistency Loss in the following subsections.

3.2 Baseline Network

In order to verify the effectiveness of our proposed sampling strategy, we choose to use RandLA-Net [Hu et al. 2020] as the baseline network model based on the following two considerations: 1) since our PCB-RS sampling method can be considered as an extension of the RS method, and RandLA-Net is the first point-based method that has achieved competitive performance on the SemanticKITTI dataset using random sampling method, it is reasonable to use RandLA-Net as baseline. 2) In [Hu et al. 2021], Hu et al. conducted ablation experiments on the SemanticKITTI dataset to evaluate the effects of different sampling strategies (FPS, IDIS, PDS,

GS, CRS, PGS) had on segmentation performance. The experimental results show that RS outperforms other sampling methods, which allows us to focus on the comparison with RS method only. It should be specially noted that our approach actually can be well embedded in other networks, and bring significant improvement as shown in Section 4 and Section 5.

3.3 Polar Cylinder Balanced Random Sampling

From previous discussion, we clearly see that the LiDAR point clouds from autonomous driving scenes have varying density, i.e. the nearby regions have much larger density than farther areas. And the simple RS strategy may not be an ideal choice for this situation, since the randomly downsampled points usually follow the same probability distribution as that of original point cloud, which means that the RS cannot deal with the unbalanced distribution problem. Figure 3 provides visualizations and statistical analysis of two cases. It can be clearly and intuitively stated that the point clouds obtained by downsampling 1/4 and 1/16 follow the same distance distribution as the original point cloud, which leads to most of the sampled points aggregating in the close-range regions. And the network with random sampling is likely to “over-fit” the point cloud at close distances and “under-fit” the points at medium and long distances.

Therefore, in order to address the problem above, we propose a new sampling method named **Polar Cylinder Balanced Random Sampling** (PCB-RS) inspired by the basic concepts of related works [Zhang et al. 2020, Zhou et al. 2020, Zhu et al. 2021]. The core idea behind our PCB-RS is that the points in the downsampled point cloud should be distributed as uniform as possible over different distance ranges, so that the segmentation model is able to learn adequate information from all distances.

The Algorithm 1 describes the detailed process of our PCB-RS, and comparison with RS method. It can be obviously reported that RS simply shuffles the input point cloud with N points, and then selects the top M points as the target point cloud to perform sampling. In contrast, PCB-RS first converts the Cartesian coordinates into the Polar coordi-

nate system, which transforms the point coordinate (x, y, z) to (ρ, θ, z) , where the radius ρ (distance to the origin of the x-y axis) and the azimuth θ (angle from the x-axis to the y-axis) are calculated. Based on this constructed Polar Coordinate System, we divide the input into different cylindrical blocks, and the farther the distance is, the larger the cells are. The right part of Figure 3 visualizes the cylindrical blocks and the number of points in each block for an example point cloud, where a long-tail distribution is observed.

Based on the number of target sampling points M and the number of cylindrical blocks K , we calculate the number of points ($S_n: K \times 1$) in each cylindrical block. During down-sampling, we attempt to balance the number of points per block, making them as the same as possible. Then we perform the sampling operations similar to RS in each cylindrical block. To be specific, we shuffle the points within each block, and select the top $S_n[i]$ points to yield a sub point cloud. After combining all the resulted sub point clouds, we perform shuffle operation once again to obtain the sampled point cloud.

Through the usage of the PCB-RS sampling method, on one hand, we are able to guarantee that the distribution of the sampled points over different distance ranges can be as uniform as possible. From the visualization in Figure 3, we find that our PCB-RS can change the point distribution with respect to distance to sensor by retaining the points at medium and long distances. More visualization samples will be provided in the supplementary material.

On the other hand, in terms of computation complexity, PCB-RS have a low computation cost since it can be considered as a collection of K sub-random sampling processes. Figure 2 presents the overall architecture of our segmentation network, where we only use PCB-RS method in the first downsampling stage, and other subsequent sampling layers still adopt RS approach. The reasons are that (1) the distribution of point clouds processed by this PCB-RS layer have been sufficiently balanced at different distances. (2) In the subsequent stages, this balance distribution can be maintained well even if they still use RS strategy for downsampling. (3) This sampling configurations makes our network efficient.

3.4 Loss and Sampling Consistency Loss

LiDAR semantic segmentation datasets often suffer from class imbalance problem. For example, in the SemanticKITTI dataset, the proportions of roads and sidewalks are hundreds of times larger than that of people and motorcycles. To handle this issue, we choose to use weighted cross-entropy loss function to better optimize these rare categories, which is formulated as,

$$\mathcal{L}_{wce} = - \sum_{c=1}^C \omega_c \cdot y_c \log(\hat{y}_c), \quad (1)$$

where C is the total number of classes in the dataset, ω_c is the calculated weight of the c th class, y_c and \hat{y}_c denote the ground truth and prediction probability, respectively.

In addition, inspired by studies [Wu et al. 2021, Li et al. 2022], we design a simple **Sampling Consistency Loss** to

Algorithm 1: Simple example algorithm of RS and PCB-RS

Input: Points with coordinates: $N \times 3$

Output: Sampling points: $M \times 3$

Random Sampling:

- 1: Random shuffle points.
- 2: Slice select the top M points.
- 3: **return** Sampling points $M \times 3$

PCB Random Sampling:

New Param: Resolution of the polar cylindrical blocks representation: $R \times P \times Z$

- 1: Convert Cartesian to Polar coordinates.
- 2: Dividing the point cloud into different cylindrical blocks based on the resolution parameter size $R \times P \times Z$.
// Here will get the number of blocks K .
- 3: Based on target sampling points M and total number of blocks K , calculate the number of points to be individually downsampled for each cylindrical block.
// Here will get a set of sample number list $S_n: K \times 1$.
- 4: *Sampling* $\leftarrow [?????]$
- 5: **for** $i \leftarrow 1$ to K **do**
- 6: Get all sub points N_i located in this block.
- 7: Get the number of points $S_n[i]$ to be sampled within the block.
- 8: Random shuffle sub points N_i .
- 9: Slice select the top $S_n[i]$ points.
- 10: Splice this subsampling point.
// e.g. *Sampling.append()*
- 11: **end for**
- 12: Random shuffle Sampling points *Sampling*.
- 13: **return** Sampling points $M \times 3$

guide the model to learn the variability of different sampling methods, and enhance the model's representation power by learning more diverse feature representations. Meanwhile it constrains the model to output a probability distribution as consistent as possible under different sampling methods. The formula for sampling consistency loss is defined as,

$$\mathcal{L}_{scl} = \sum_{c=1}^C |\hat{y}_c^{PCB-RS} - \hat{y}_c^{RS}|, \quad (2)$$

where \hat{y}_c^{PCB-RS} and \hat{y}_c^{RS} are the predicted probabilities obtained by using PCB-RS and RS, respectively. The total loss \mathcal{L}_{total} is the weighed sum of these two loss functions, formulated as,

$$\mathcal{L}_{total} = \mathcal{L}_{wce} + \alpha \mathcal{L}_{scl} \quad (3)$$

However, such a loss formula leads to a more tedious optimal weighted hyperparameter search process. In order to solve this problem, we introduce the uncertainty weighting method proposed by [Kendall, Gal, and Cipolla 2018], which automatically adjusts the optimal ratio between different loss terms by introducing two learnable parameters σ_1 and σ_2 . And we also add two additional logarithmic regular terms to maintain stability. The total loss can be written

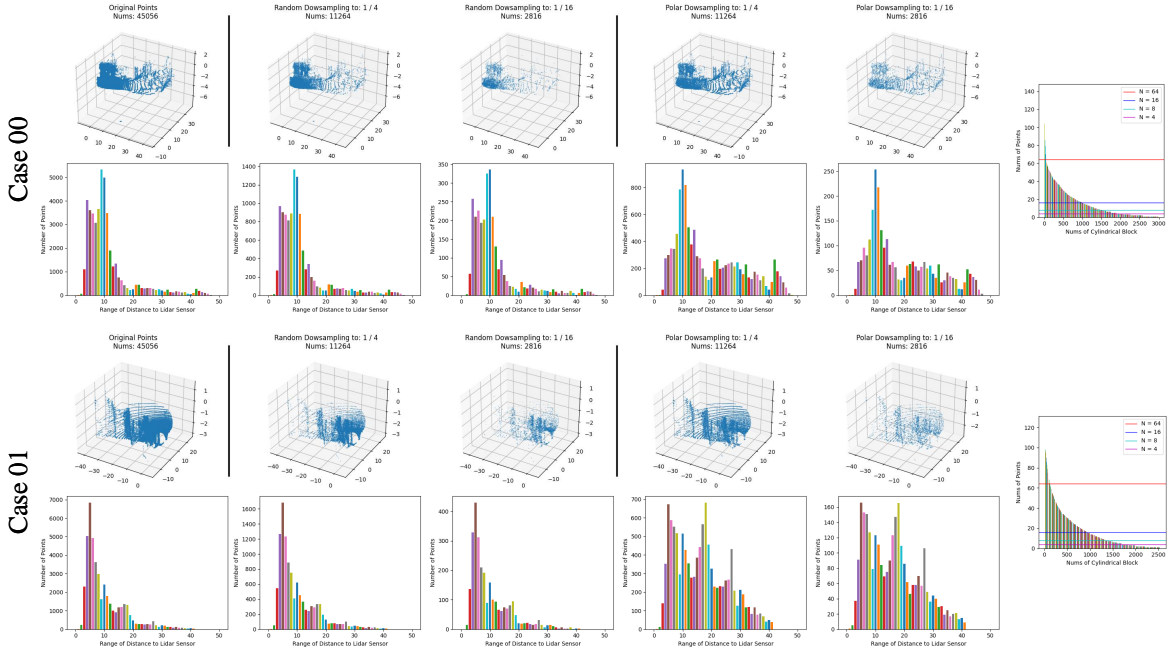


Figure 3: Comparison of qualitative visualization and quantitative statistical analysis between RS and PCB-RS. In each subcase, the upper part shows the visualization of the point cloud, and the lower part shows the distribution of that point cloud at different distance ranges. The subplot on the right shows the distribution of the number of points within the cylindrical block when using the PCB-RS method. *Best viewed in color and zoomed in for more detail.*

as follows,

$$\begin{aligned} \mathcal{L}_{total} = & \frac{1}{\sigma_1^2} \mathcal{L}_{wce} + \frac{1}{\sigma_2^2} \mathcal{L}_{scl} \\ & + \log(1 + \sigma_1) + \log(1 + \sigma_2), \end{aligned} \quad (4)$$

4 Experiments

To verify the effectiveness of our approach, we evaluate it on two benchmarks, SemanticKITTI [Behley et al. 2019] and SemanticPOSS [Pan et al. 2020].

SemanticKITTI is currently the largest dataset for the task of point cloud segmentation in autonomous driving scenes. With vehicles equipped with Velodyne HDL-64E rotating LIDAR, 43,552 LIDAR scans from 22 sequences were collected from a German city and labeled with dense point-based annotations. Sequences 00 to 10 (19,130 scans) were used for training, sequence 08 (4,071 scans) for validation, and sequences 11 to 21 (20,351 scans) for testing.

SemanticPOSS is a smaller, sparser, and more challenging benchmark collected by Peking University through the Hesai Pandar LiDAR sensor within the campus environment. It consists of 2,988 different, complex LiDAR scenes, each with a large number of sparse dynamic instances (e.g., person and rider). SemanticPOSS is divided into 6 LiDAR data sequences. We follow the official division by using 03 sequences as tests and the rest for training.

Implementation details. We perform all experiments on a single RTX 3090 GPU. During training, we use the same experimental setup as the RandLA-Net. The network is trained

for 100 epochs using Adam as the optimizer. The initial learning rate is set to 0.01 and reduced by 5% after each epoch.

For both datasets, the resolution of the polar cylinder representation used in PCB-RS is set to $64 \times 64 \times 16$, where these three dimensions correspond to radius, angle, and height, respectively. For SemanticKITTI, we keep the point cloud in the range of $[distance : 3 \sim \max(\cdot)m, z : -3.0 \sim 1.5m]$. For SemanticPOSS, the point cloud is kept in the range of $[distance : 3 \sim 80m, z : -3.0 \sim 3m]$.

It should be noted that in order to make a fair comparison, we re-implement RandLA-Net [Hu et al. 2020], BAF-LAC [Shuai, Xu, and Liu 2021] and BAAF [Qiu, Anwar, and Barnes 2021] based on the PyTorch framework.

4.1 Semantic Segmentation Results

Results on SemanticKITTI: Table 1 shows the segmentation performance of our proposed method compared with the baseline method for different distance ranges. The experimental results show that our proposed method can improve the segmentation performance of the model at different distance ranges. Specifically, our proposed PCB-RS method brings 1.9%, 2.2%, and 1.9% mIoU performance improvement over the baseline RS sampling method in the three medium and long distance ranges ($30m \sim 40m$, $40m \sim 50m$, and $>50m$), respectively. Combined with the SCL module, the model further achieves performance improvements of 2.3%, 2.3%, 3.1%, 5.5%, 4.2%, and 4.6% mIoU in each of the six distance interval ranges.

Table 1: Evaluation results on SemanticKITTI validation set at different distance ranges.

	Method	mIoU(%)																			
	RS	55.9	96.1	13.3	32.6	61.1	45.5	59.6	76.0	0.0	94.2	43.9	81.8	0.0	86.4	59.1	85.6	71.8	70.1	62.8	22.4
Range From 0 m to 10 m	PCB-RS	58.9	96.4	11.2	51.0	75.8	53.3	65.8	84.1	0.0	93.5	42.6	83.1	0.0	87.9	61.1	86.6	67.7	74.9	58.6	25.5
	PCB-RS+SCL	58.2	95.7	5.8	41.4	86.5	40.2	52.0	83.8	0.0	94.7	42.7	84.7	0.0	85.8	64.9	89.1	73.8	76.5	67.3	20.4
	RS	52.6	93.3	14.2	16.7	65.2	28.4	51.5	66.5	0.0	91.0	43.9	70.4	1.6	91.2	33.1	84.1	68.0	71.5	54.6	54.9
Range From 10 m to 20 m	PCB-RS	51.4	90.6	15.8	24.2	25.1	32.9	49.6	78.8	0.0	91.8	45.6	72.4	0.0	91.6	33.4	83.0	64.1	69.5	54.3	54.0
	PCB-RS+SCL	54.9	94.2	10.1	18.1	58.2	36.3	51.1	82.2	0.0	92.9	47.3	74.4	0.1	92.1	40.6	85.9	70.4	71.9	59.2	57.7
	RS	44.6	82.4	2.0	4.2	76.9	18.6	29.8	47.9	0.0	82.4	29.9	54.6	1.3	86.9	20.5	82.0	57.6	72.7	46.6	51.3
Range From 20 m to 30 m	PCB-RS	45.5	84.2	7.6	13.5	70.5	24.6	37.5	41.0	0.0	84.4	32.4	56.6	0.0	87.8	21.3	80.5	54.6	70.5	46.5	50.7
	PCB-RS+SCL	47.7	88.0	2.7	12.0	74.2	21.6	38.0	46.8	0.0	86.0	33.4	58.4	0.5	89.2	28.6	85.7	63.6	72.2	49.2	55.6
	RS	31.4	58.2	1.6	0.6	22.1	16.5	14.1	8.8	0.0	71.4	16.1	38.3	8.6	81.3	11.4	78.6	44.5	63.9	36.6	23.3
Range From 30 to 40 m	PCB-RS	33.3	64.8	1.5	0.0	21.8	20.9	20.4	16.7	0.0	74.1	17.1	41.4	2.2	83.4	14.4	80.6	44.1	65.3	38.3	26.0
	PCB-RS+SCL	36.9	72.5	1.2	1.5	37.0	16.6	19.0	31.1	0.0	77.1	15.8	42.0	7.5	85.6	17.9	85.5	52.4	68.4	41.3	28.4
	RS	23.3	38.8	0.0	0.0	4.2	15.9	2.5	1.1	0.0	61.3	9.0	25.8	4.2	77.4	6.8	77.3	32.0	52.7	23.5	11.0
Range From 40 to 50 m	PCB-RS	25.5	45.9	0.1	0.0	12.4	15.3	2.7	2.0	0.0	62.2	9.1	30.1	0.2	80.9	9.2	80.2	36.0	57.6	26.4	13.8
	PCB-RS+SCL	27.5	52.0	0.1	0.0	13.5	15.7	4.5	2.0	0.0	66.3	5.2	29.0	5.4	83.4	11.3	84.9	40.5	60.3	31.6	16.6
	RS	9.5	13.6	0.0	0.0	0.0	5.6	0.0	0.0	0.0	18.8	2.6	9.9	0.0	16.3	2.0	68.5	3.5	23.7	16.4	0.0
Range Above 50 m	PCB-RS	11.4	15.7	0.0	0.0	0.0	7.3	0.0	0.0	0.0	21.0	0.7	11.6	0.0	18.1	1.2	78.1	6.1	34.8	22.2	0.0
	PCB-RS+SCL	14.1	27.2	0.0	0.0	0.0	0.7	0.0	0.0	0.0	26.1	0.4	7.7	0.0	22.2	6.5	88.7	15.1	40.5	32.0	0.0
	RS	53.7	93.7	12.4	27.8	61.6	39.8	51.1	69.2	0.0	92.4	41.8	77.3	2.5	88.2	48.0	84.3	64.6	70.2	56.1	38.9
Total Range	PCB-RS	55.3	93.8	12.4	42.3	57.7	46.4	54.6	77.3	0.0	92.2	41.3	78.9	0.2	89.2	50.6	84.6	61.2	72.5	54.4	40.3
	PCB-RS+SCL	56.5	94.5	6.8	35.5	76.7	37.6	48.3	79.0	0.0	93.4	42.4	80.8	1.1	89.0	56.9	87.6	68.4	74.4	61.0	40.8

Table 2: Evaluation results on the SemanticPOSS dataset. \dagger : result reported by Pan et al. \ddagger : result reported by Li, Liu, and Gall and Li et al. $*$: result reported by our implementation.

	person	rider	car	trunk	plants	traffic sign	pole	building	fence	bike	road	mIoU
PointNet++ \dagger [Qi et al. 2017a]	20.8	0.1	8.9	40.9	51.2	21.8	3.2	42.7	6.0	0.1	62.2	20.1
SqueezeSegV2 \dagger [Wu et al. 2019]	18.4	11.2	34.9	15.8	56.3	11.0	4.5	47.0	25.5	32.4	71.3	29.8
RangeNet33 \ddagger [Milillo et al. 2019]	10.0	6.2	33.4	7.3	54.2	5.6	2.6	49.9	18.4	28.6	63.5	25.4
RangeNet33 + KNN \ddagger [Milillo et al. 2019]	14.2	8.2	35.4	9.2	58.1	6.8	2.8	55.5	28.8	32.2	66.3	28.9
UnPNC + KNN \ddagger [Li, Liu, and Gall 2021]	11.3	12.1	36.8	10.6	62.3	6.9	4.2	60.4	20.6	35.4	65.5	29.7
MINet + KNN \ddagger [Li, Liu, and Gall 2021]	17.7	17.2	39.2	13.8	67.0	9.5	5.8	66.9	31.1	40.5	68.4	34.3
MINet + KNN \ddagger [Li et al. 2021]	13.3	11.3	34.0	18.8	62.9	11.8	4.1	55.5	20.4	34.7	69.2	30.5
SalsaNext \ddagger [Cortinhal, Tzelepis, and Aksoy 2020]	20.1	15.1	36.0	23.4	67.4	15.5	5.1	61.6	28.2	40.2	72.9	35.1
SalsaNext + KNN \ddagger [Cortinhal, Tzelepis, and Aksoy 2020]	62.6	49.8	63.5	34.7	78.0	39.1	26.7	79.4	54.7	54.2	83.1	56.9
FIDNet \ddagger [Zhao, Bai, and Huang 2021]	58.1	44.5	69.3	39.9	76.6	36.4	23.6	76.5	59.6	53.4	81.7	56.3
FIDNet + KNN \ddagger [Zhao, Bai, and Huang 2021]	58.6	45.1	70.0	40.2	76.9	37.3	23.5	77.1	59.1	53.1	83.3	56.6
BAF-LAC [†] (Baseline with RS)	50.4	48.7	54.4	40.0	72.5	22.4	28.1	74.5	42.0	48.8	81.0	51.2
BAF-LAC (PCB-RS)	52.9	54.1	44.5	35.7	73.5	28.9	42.8	78.9	52.2	49.1	82.2	54.1
PCB-BAF-LAC (PCB-RS + SCL)	56.4	57.7	53.8	43.5	73.9	32.1	43.3	72.5	52.8	51.4	83.8	56.5
BAAF [†] (Baseline with RS)	53.4	56.1	53.8	45.3	74.3	32.7	30.7	74.7	43.4	53.6	81.9	54.4
BAAF (PCB-RS)	56.7	57.6	60.5	45.8	77.6	37.0	36.5	81.4	48.7	50.4	83.7	57.8
PCB-BAAF (PCB-RS + SCL)	58.1	57.6	63.2	41.8	77.9	28.9	33.8	79.8	60.1	52.2	84.9	58.0
RandLA-Net [†] (Baseline with RS)	56.8	58.2	48.1	37.8	73.4	22.3	35.4	76.6	45.4	45.7	80.9	52.8
RandLA-Net (PCB-RS)	55.9	53.8	58.9	44.7	77.5	34.5	27.7	82.8	42.6	49.9	82.0	55.5
PCB-RandNet (PCB-RS + SCL)	57.7	52.4	61.4	42.0	78.1	31.8	33.0	81.6	51.5	51.2	84.3	56.8

Results on SemanticPOSS: Table 2 shows the comparison of our proposed method with other related works and baseline. To make a fair comparison, we also reproduce and report the results of two more recent and powerful models, SalsaNext [Cortinhal, Tzelepis, and Aksoy 2020] and FIDNet [Zhao, Bai, and Huang 2021], on the SemanticPOSS dataset. Experimental results show that the proposed PCB-RS sampling method and SCL loss actually contribute to significant improvements on more challenging dataset with much smaller objects.

Specifically, for the baseline approach **RandLA-Net**, the introductions of PCB-RS and SCL help achieve mIoU improvements of 2.7% and 1.3%, respectively, and their combination improves the segmentation performance from 52.8% to 56.8%. For **BAF-LAC**, the usage of PCB-RS and

SCL makes improvements of 2.9% and 2.4% mIoU, respectively, and they together improve the performance from 51.2% to 56.5%. For **BAAF**, PCB-RS and SCL improve the mIoU by 2.4% and 1.0%, respectively. The segmentation performance obtained by integrating both PCB-RS and SCL is increased from 54.4% to 58.0%.

5 Ablation Study

We conducted the following ablation experiments on the SemanticKITTI dataset to quantify the effectiveness of the different components. To perform efficient training and evaluation, the training and validation sets are built by selecting one frame from the original sequence with every 3 frames interval. i.e. only 25% of the original training and validation data used.

Effects of Polar Cylinder Balanced Random Sampling. Table 3 shows the segmentation performance of our model at different distance ranges with different sampling methods. Considering the randomness of the whole framework, the results under 3 different random seeds are reported for a fairer comparison. These results show that: 1) The segmentation performance decreases sharply as the distance to the center LiDAR sensor increases. 2) Compared to baseline RS, our proposed PCB-RS sampling method achieves remarkable performance improvements in both medium and long ranges. This is consistent with our expectation that PCB-RS can preserve the points at medium and long distances well. 3) Surprisingly, PCB-RS achieves moderate improvement in the close range ($<10m$). We think it is due to the overfitting of the model, and most of the points obtained after RS sampling mainly aggregate in the closer regions, and the net-

Table 3: Comparison of mean IoU (%) for different distance ranges and overall on the SemanticKITTI validation set.

	Seed											
	143			520			1024					
	RS	PCB-RS	Improv	RS	PCB-RS	Improv	RS	PCB-RS	Improv	RS	PCB-RS	Improv
Range From 0 m to 10 m	56.67	58.56	+1.89	55.71	58.24	+2.53	54.85	58.63	+3.78			
Range From 10 m to 20 m	49.80	52.84	+3.04	51.25	53.62	+2.37	50.96	51.32	+0.36			
Range From 20 m to 30 m	40.06	43.83	+3.77	39.83	44.14	+4.31	38.44	42.33	+3.89			
Range From 30 m to 40 m	28.94	33.06	+4.12	30.10	33.28	+3.18	28.36	31.62	+3.26			
Range From 40 m to 50 m	21.46	25.76	+4.30	22.51	24.96	+2.45	21.71	23.78	+2.07			
Range Above 50 m	8.25	12.17	+3.92	9.90	11.42	+1.52	8.62	11.18	+2.56			
Total Range	52.81	55.61	+2.80	52.65	55.61	+2.96	52.02	55.04	+3.02			

Table 4: Comparison of the time cost of different sampling methods. For a fair comparison, all methods are tested based on the numpy [Harris et al. 2020] implementation.

Downsampling	Test case 1			Test case 2		
	Sampling Way					
	RS	PCB-RS	FPS	RS	PCB-RS	FPS
(4096→1024) × 11	0.00149	0.17094	8.01109	0.00153	0.17525	8.08017
(4096→1024→256) × 11	0.00147	0.16849	8.60692	0.00151	0.17105	8.52015
(4096→1024→256→64) × 11	0.00149	0.16845	8.54591	0.00143	0.16765	8.49970
(4096→1024→256→64→16) × 11	0.00149	0.16898	8.79153	0.00143	0.16774	8.47435

work is likely to overfit these closer features, which leads to performance degradation.

Time Consumption Comparison. Table 4 shows the time consumption of different sampling methods for downsampling the input point cloud. Results demonstrate that the RS is the fastest method, while the FPS sampling approach requires very high time consumption due to its high computation complexity. In contrast, our proposed PCB-RS can maintain a relatively ideal time consumption. Additionally, we observe that the time cost of the RS method is almost constant (within the error margin), while FPS’s time consumption is increasing when performing multiple downsampling. As for our PCB-RS, it can be expected that the time cost inevitably increase as well but not significantly. However, to maintain a stable time consumption, we replace only the first RS with PCB-RS in our network as discussed in the previous Section 3.3.

Effects of Sampling Consistency Loss. Here, we conduct further experiments to validate the effectiveness of the proposed sampling consistency loss and uncertainty weighting methods. As shown in Table 5, fixed weighting weights only lead to slight performance improvements or even performance degradation, while the learnable weighting method shown in Equation 4 can bring significantly better performance. Moreover, the validation results on the sub-sample set show that the introduction of sampling consistency loss can reduce the performance variance of the model under different sampling methods, and the learnable weighting method can reduce this variance (from 1.99% miou to 1.07% miou).

Consistent Effectiveness under Different Baselines. We have verified the effectiveness of PCB-RS and SCL on three different baseline networks (RandLA-Net, BAF-LAC and BAAF) on the SemanticPOSS dataset in Section 4.1. However, considering the obvious domain differences or sensor differences between the SemanticKITTI and Semantic

Table 5: Evaluation of sampling consistency loss and uncertainty weighting method.

Loss Function	mIoU on val set		mIoU on subsample set		
	PCB-RS	RS	PCB-RS	Gap	
\mathcal{L}_{wce}	55.04	48.48	50.47	1.99	
$\mathcal{L}_{wce} + 10 * \mathcal{L}_{scl}$	55.34	50.14	51.44	1.30	
$\mathcal{L}_{wce} + 15 * \mathcal{L}_{scl}$	54.69	51.01	52.39	1.38	
Equation 4	57.16	53.07	54.14	1.07	

Table 6: Evaluation of PCB-RS and SCL on different baselines.

	BAF-LAC (Baseline with RS)	BAF-LAC (PCB-RS)	Improv	PCB-BAF-LAC (PCB-RS+SCL)	Improv
	BAAF (Baseline with RS)	BAAF (PCB-RS)	Improv	PCB-BAAF (PCB-RS+SCL)	Improv
Range From 0 m to 10 m	56.44	57.50	+1.06	56.96	+0.52
Range From 10 m to 20 m	49.74	51.84	+2.10	53.44	+3.70
Range From 20 m to 30 m	39.23	42.05	+2.82	44.98	+5.75
Range From 30 m to 40 m	28.71	32.89	+4.15	36.30	+7.59
Range From 40 m to 50 m	22.89	25.02	+2.13	27.03	+4.14
Range Above 50 m	9.80	11.11	+1.31	13.10	+3.30
Total Range	52.96	54.65	+1.69	55.16	+2.20
	BAAF (Baseline with RS)	BAAF (PCB-RS)	Improv	PCB-BAAF (PCB-RS+SCL)	Improv
Range From 0 m to 10 m	55.47	57.71	+2.24	57.96	+2.49
Range From 10 m to 20 m	50.74	51.25	+0.51	52.68	+1.94
Range From 20 m to 30 m	40.32	42.59	+2.27	45.24	+4.92
Range From 30 m to 40 m	29.37	31.23	+1.86	34.30	+4.93
Range From 40 m to 50 m	21.57	22.97	+1.40	24.78	+3.21
Range Above 50 m	10.49	9.84	-0.65	13.13	+2.64
Total Range	52.53	54.20	+1.67	55.58	+3.05

ticPOSS datasets, it is necessary to perform validation on the SemanticKITTI dataset. In order to avoid the excessive time and resource consumption required for training with the whole data, we only perform fast validation on a smaller sub-sample dataset in the ablation experiment. The experimental results in Table 6 show that our PCB-RS sampling method and SCL loss make the BAF-LAC and BAAF achieve consistent enhancement results. Meanwhile, as we expected, the improvement of the model at medium and long distances is more obvious.

Limitation: The limitations of our proposed method, as well as additional experimental analysis and visualization results, will be illustrated in the supplementary material.

6 Conclusion

In this paper, we propose a novel sampling method, called Polar Cylinder Balanced Random Sampling, for the autonomous driving LiDAR point cloud segmentation task. The PCB-RS sampling method enables the sampled point clouds to maintain a more balanced distribution and guides the network to fully learn the point cloud features at different distances. We also propose a sampling consistency loss to further improve the model performance and reduce the variance of the model under different sampling methods. Experimental results on SemanticKITTI and SemanticPOSS show that our proposed approach achieves consistent performance improvements and enhances the segmentation performance of the model at different distance ranges.

References

Behley, J.; Garbade, M.; Milioto, A.; Quenzel, J.; Behnke, S.; Stachniss, C.; and Gall, J. 2019. Semantic3D: A dataset for semantic scene understanding of lidar sequences. In *ICCV*, 9297–9307. [5](#)

Choy, C.; Gwak, J.; and Savarese, S. 2019. 4d spatio-temporal convnets: Minkowski convolutional neural networks. In *CVPR*, 3075–3084. [1, 2](#)

Cortinhal, T.; Tzelepis, G.; and Aksoy, E. E. 2020. Sal-saNext: Fast, uncertainty-aware semantic segmentation of LiDAR point clouds. In *International Symposium on Visual Computing*, 207–222. [6](#)

Feng, D.; Haase-Schütz, C.; Rosenbaum, L.; Hertlein, H.; Glaeser, C.; Timm, F.; Wiesbeck, W.; and Dietmayer, K. 2020. Deep multi-modal object detection and semantic segmentation for autonomous driving: Datasets, methods, and challenges. *IEEE Trans. Intell. Transp. Syst.*, 22(3): 1341–1360. [1](#)

Geiger, A.; Lenz, P.; and Urtasun, R. 2012. Are we ready for autonomous driving? the kitti vision benchmark suite. In *CVPR*, 3354–3361. [1](#)

Harris, C. R.; Millman, K. J.; Van Der Walt, S. J.; Gommers, R.; Virtanen, P.; Cournapeau, D.; Wieser, E.; Taylor, J.; Berg, S.; Smith, N. J.; et al. 2020. Array programming with NumPy. *Nature*, 585(7825): 357–362. [7](#)

Hu, Q.; Yang, B.; Xie, L.; Rosa, S.; Guo, Y.; Wang, Z.; Trigoni, N.; and Markham, A. 2020. Randla-net: Efficient semantic segmentation of large-scale point clouds. In *CVPR*, 11108–11117. [2, 3, 5](#)

Hu, Q.; Yang, B.; Xie, L.; Rosa, S.; Guo, Y.; Wang, Z.; Trigoni, N.; and Markham, A. 2021. Learning semantic segmentation of large-scale point clouds with random sampling. *IEEE Trans. Pattern Anal. Mach. Intell.* [3](#)

Kendall, A.; Gal, Y.; and Cipolla, R. 2018. Multi-task learning using uncertainty to weigh losses for scene geometry and semantics. In *CVPR*, 7482–7491. [4](#)

Li, S.; Chen, X.; Liu, Y.; Dai, D.; Stachniss, C.; and Gall, J. 2021. Multi-scale interaction for real-time lidar data segmentation on an embedded platform. *IEEE Robot. Autom. Lett.*, 7(2): 738–745. [6](#)

Li, S.; Liu, Y.; and Gall, J. 2021. Rethinking 3-D LiDAR Point Cloud Segmentation. *IEEE Trans. Neural Netw. Learn. Syst.* [6](#)

Li, X.; Zhang, G.; Pan, H.; and Wang, Z. 2022. CPGNet: Cascade Point-Grid Fusion Network for Real-Time LiDAR Semantic Segmentation. In *ICRA*. [4](#)

Li, Y.; Bu, R.; Sun, M.; Wu, W.; Di, X.; and Chen, B. 2018. Pointcnn: Convolution on x-transformed points. *NeurIPS*, 31. [2](#)

Milioto, A.; Vizzo, I.; Behley, J.; and Stachniss, C. 2019. Rangenet++: Fast and accurate lidar semantic segmentation. In *IROS*, 4213–4220. [1, 2, 6](#)

Pan, Y.; Gao, B.; Mei, J.; Geng, S.; Li, C.; and Zhao, H. 2020. Semantic3D: A point cloud dataset with large quantity of dynamic instances. In *IV*, 687–693. [5, 6](#)

Qi, C. R.; Su, H.; Mo, K.; and Guibas, L. J. 2017a. Pointnet: Deep learning on point sets for 3d classification and segmentation. In *CVPR*, 652–660. [1, 2, 6](#)

Qi, C. R.; Yi, L.; Su, H.; and Guibas, L. J. 2017b. Pointnet++: Deep hierarchical feature learning on point sets in a metric space. *NeurIPS*, 30. [1, 2](#)

Qiu, S.; Anwar, S.; and Barnes, N. 2021. Semantic segmentation for real point cloud scenes via bilateral augmentation and adaptive fusion. In *CVPR*, 1757–1767. [3, 5](#)

Shuai, H.; Xu, X.; and Liu, Q. 2021. Backward Attentive Fusing Network With Local Aggregation Classifier for 3D Point Cloud Semantic Segmentation. *IEEE Transactions on Image Processing*, 30: 4973–4984. [3, 5](#)

Tang, H.; Liu, Z.; Zhao, S.; Lin, Y.; Lin, J.; Wang, H.; and Han, S. 2020. Searching efficient 3d architectures with sparse point-voxel convolution. In *ECCV*, 685–702. [2](#)

Thomas, H.; Qi, C. R.; Deschaud, J.-E.; Marcotegui, B.; Goulette, F.; and Guibas, L. J. 2019. Kpconv: Flexible and deformable convolution for point clouds. In *ICCV*, 6411–6420. [2](#)

Wu, B.; Wan, A.; Yue, X.; and Keutzer, K. 2018. Squeeze-seg: Convolutional neural nets with recurrent crf for real-time road-object segmentation from 3d lidar point cloud. In *ICRA*, 1887–1893. [1, 2](#)

Wu, B.; Zhou, X.; Zhao, S.; Yue, X.; and Keutzer, K. 2019. SqueezeSegv2: Improved model structure and unsupervised domain adaptation for road-object segmentation from a lidar point cloud. In *ICRA*, 4376–4382. [2, 6](#)

Wu, L.; Li, J.; Wang, Y.; Meng, Q.; Qin, T.; Chen, W.; Zhang, M.; Liu, T.-Y.; et al. 2021. R-drop: Regularized dropout for neural networks. *NeurIPS*, 34: 10890–10905. [4](#)

Wu, W.; Qi, Z.; and Fuxin, L. 2019. Pointconv: Deep convolutional networks on 3d point clouds. In *CVPR*, 9621–9630. [2](#)

Xu, C.; Wu, B.; Wang, Z.; Zhan, W.; Vajda, P.; Keutzer, K.; and Tomizuka, M. 2020. SqueezeSegv3: Spatially-adaptive convolution for efficient point-cloud segmentation. In *ECCV*, 1–19. [2](#)

Yan, X.; Gao, J.; Li, J.; Zhang, R.; Li, Z.; Huang, R.; and Cui, S. 2021. Sparse single sweep lidar point cloud segmentation via learning contextual shape priors from scene completion. In *AAAI*, volume 35, 3101–3109. [2](#)

Yan, X.; Zheng, C.; Li, Z.; Wang, S.; and Cui, S. 2020. Pointasnl: Robust point clouds processing using nonlocal neural networks with adaptive sampling. In *CVPR*, 5589–5598. [2, 3](#)

Zhang, Y.; Zhou, Z.; David, P.; Yue, X.; Xi, Z.; Gong, B.; and Foroosh, H. 2020. Polarnet: An improved grid representation for online lidar point clouds semantic segmentation. In *CVPR*, 9601–9610. [2, 3](#)

Zhao, Y.; Bai, L.; and Huang, X. 2021. FIDNet: LiDAR Point Cloud Semantic Segmentation with Fully Interpolation Decoding. In *IROS*, 4453–4458. [6](#)

Zhou, H.; Zhu, X.; Song, X.; Ma, Y.; Wang, Z.; Li, H.; and Lin, D. 2020. Cylinder3d: An effective 3d framework for

driving-scene lidar semantic segmentation. *arXiv preprint arXiv:2008.01550*. [2](#), [3](#)

Zhu, X.; Zhou, H.; Wang, T.; Hong, F.; Ma, Y.; Li, W.; Li, H.; and Lin, D. 2021. Cylindrical and asymmetrical 3d convolution networks for lidar segmentation. In *CVPR*, 9939–9948.

[3](#)

Supplementary Material

A Limitation and Future Work

Limitation of PCB-RS

PCB-RS may have the following problems:

- During the algorithmic flow of PCB-RS, since the cylindrical blocks and the number of points in each block shows a long-tailed distribution, taking out a certain number of points from different cylindrical blocks can be considered a typical long-tailed distribution problem. We used a strategy of forced balancing (i.e. balancing the number of points per block so that they are as equal as possible) to deal with this problem. However, whether there is a better way to deal with this problem is our further future work.
- We implement the PCB-RS method based on vanilla Python and Numpy, so in the ablation experiments section of the main text, we compare the RS and FPS sampling methods implemented in the same way. For the RS method, this comparison is fair. Because in RandLA-Net [Hu et al. 2020], it's also implemented using NumPy. However, the FPS method can achieve faster speeds with an efficient CUDA implementation. Therefore, the comparison with FPS is “*potentially unfair*”. Faster implementations of PCB-RS (e.g. CUDA, Numba) will also be seen as further work.

Limitation of SCL

The main limitation of Sampling Consistency Loss comes from the larger GPU memory consumption and longer training time. However, as shown by the dashed line in the network structure figure in main text, our Sampling Consistency Loss is only utilized during training and discarded during inference, i.e., it is disposable. Therefore, it does not introduce any computational burden during inference.

Limitation of our method

Since we only study the effect of the sampling method in this paper, we do not make any adjustments to the baseline network structure [Hu et al. 2020, Shuai, Xu, and Liu 2021, Qiu, Anwar, and Barnes 2021]. However, the point cloud distributions under RS and PCB-RS sampling methods are very different. Therefore it is necessary to design more suitable local feature extraction and local feature aggregation operators for PCB-RS sampling. This will be considered as our future work.

B More visualization and statistical analysis comparisons between RS and PCB-RS

Figure 2 shows more examples of comparisons between RS and PCB-RS similar to those in the main text. These visualizations show that PCB-RS can change the point distribution with respect to distance to sensor by retaining the points at medium and long distances.

C Ablation studies about Resolution of Polar Cylinder

Ablation studies about resolution of the polar cylinder representation are reported in Table 1. The results show that PCB-RS is relatively robust to the size setting of the resolution of polar cylinder.

Table 1: Effect of Resolution of Polar Cylinder on SemanticKITTI validation set.

Resolution of Polar Cylinder	None (Baseline with RS)	32×32×16	48×48×16	64×64×16	96×96×32
mIoU(%)	52.02	54.34	54.67	55.04	53.46

D Qualitative results comparison on SemanticKITTI validation set

Figure 2 shows qualitative visualization of the segmentation results of our method compared to the baseline on the SemanticKITTI validation set. Compared to the baseline, our method has fewer false predictions, while the improvement is more significant at medium and long distances.

E Quantitative results comparison on SemanticPOSS dataset

The visualization analysis in Figure 3 shows that our method achieves better segmentation performance at different baselines for different distance ranges on SemanticPOSS dataset, which is precisely the result expected from our new PCB-RS sampling method and SCL loss. Table 2, 3, 4 further list the segmentation performance improvement of our proposed method for different distance ranges when RandLA-Net [Hu et al. 2020], BAAF [Qiu, Anwar, and Barnes 2021], BAF-LAC [Shuai, Xu, and Liu 2021] is used as the baseline.

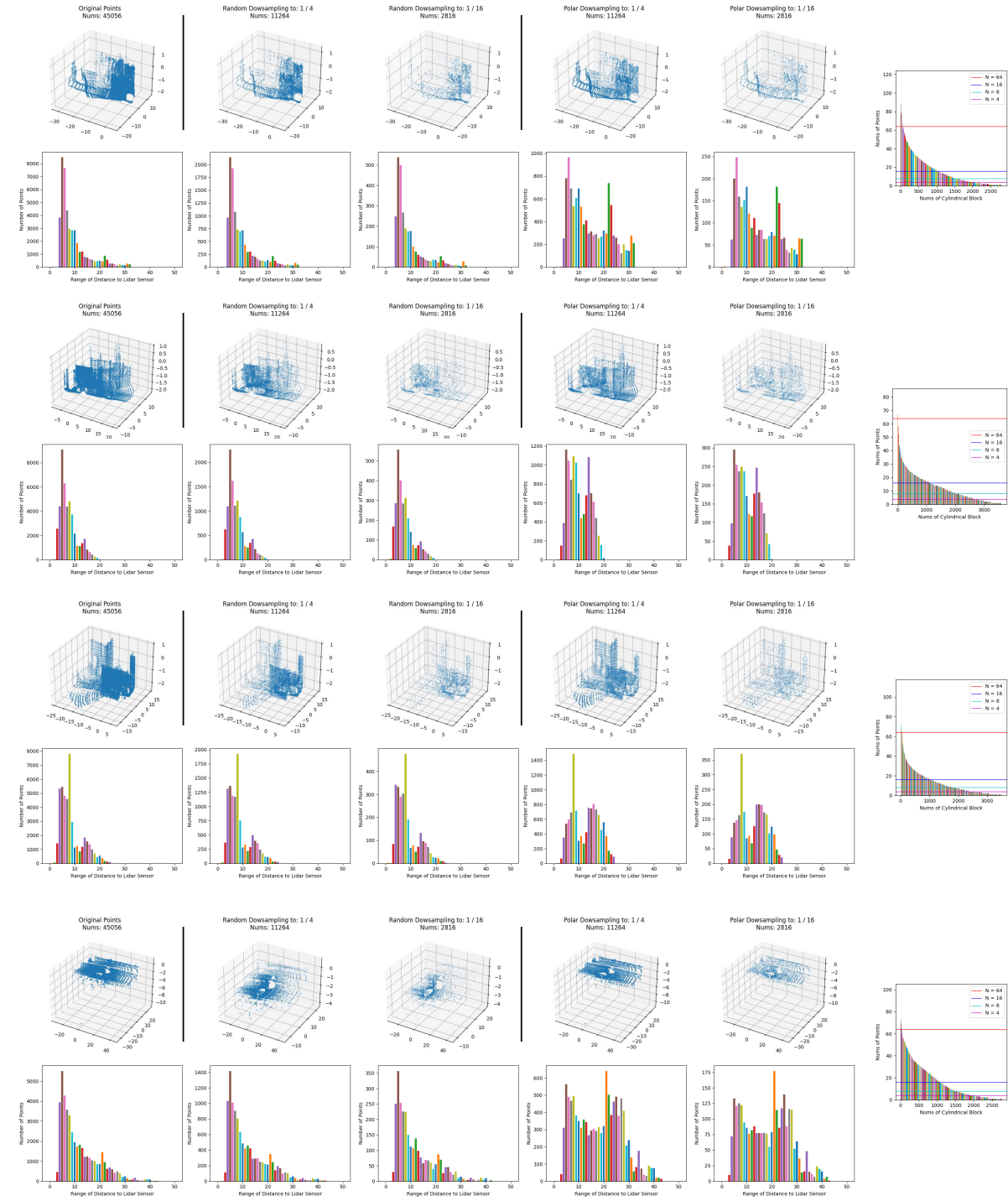


Figure 1: Comparison of qualitative visualization and quantitative statistical analysis between RS and PCB-RS. In each subcase, the upper part shows the visualization of the point cloud, and the lower part shows the distribution of that point cloud at different distance ranges. The subplot on the right shows the distribution of the number of points within the cylindrical block when using the PCB-RS method. *Best viewed in color and zoomed in for more detail.*

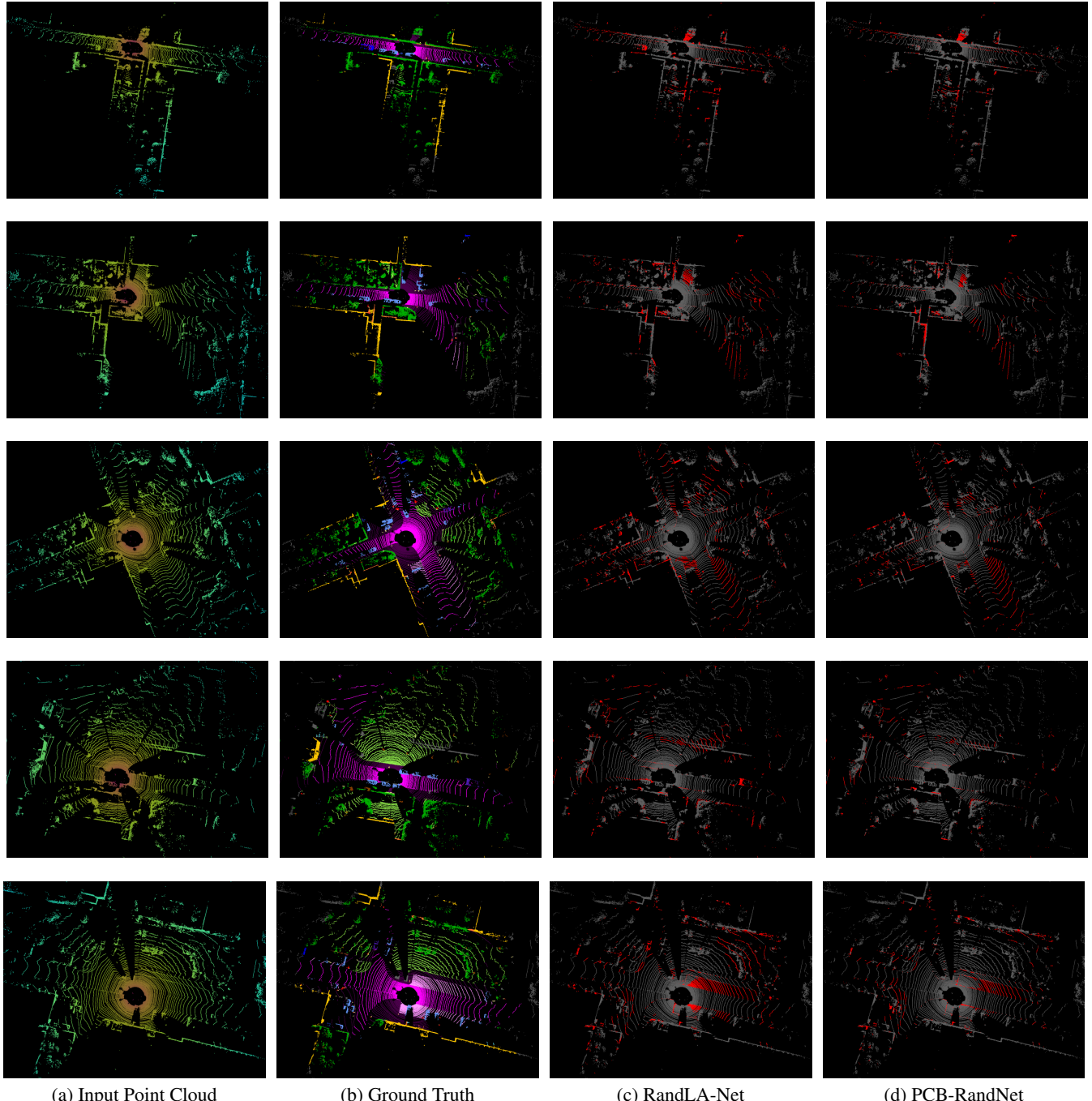
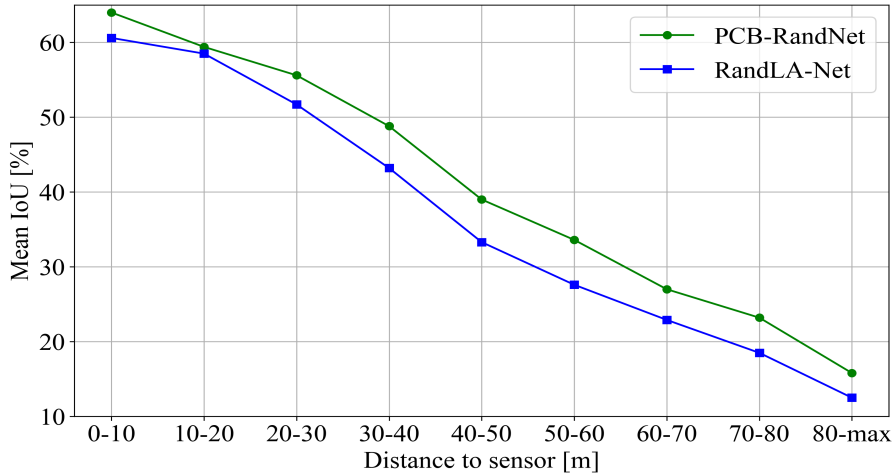
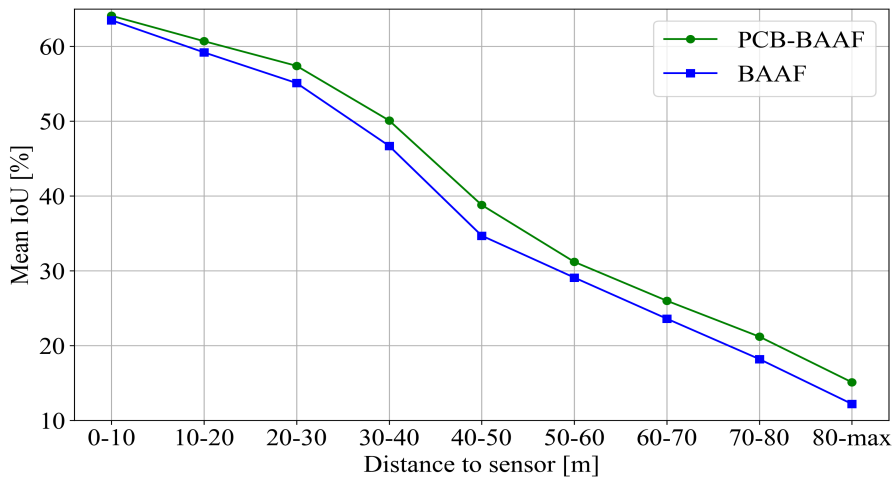


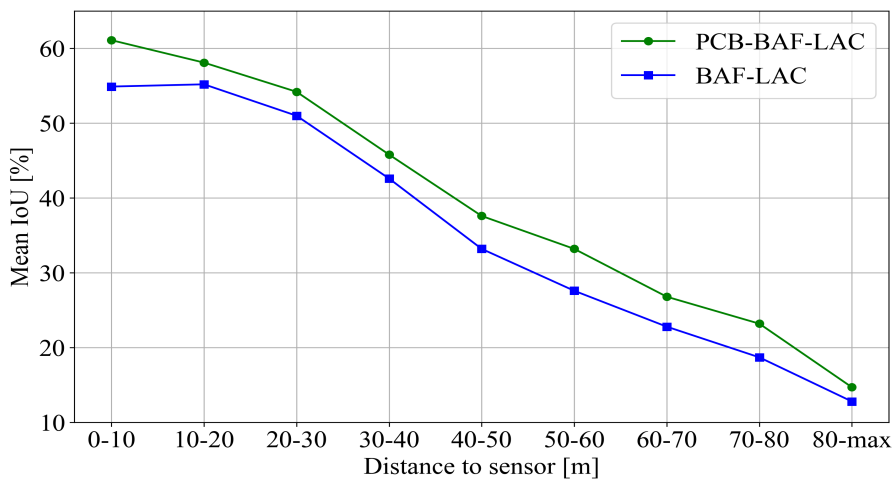
Figure 2: Qualitative analysis on SemanticKITTI validation set. Where (a) and (b) are input data of the LIDAR scan frame and corresponding segmentation ground truth, (c) and (d) are segmentation error maps in this scan frame for baseline and our method. (With red indicating wrong prediction)



(a) Baseline: RandLA-Net [Hu et al. 2020]



(b) Baseline: BAAF [Qiu, Anwar, and Barnes 2021]



(c) Baseline: BAF-LAC [Shuai, Xu, and Liu 2021]

Figure 3: Evaluation of segmentation performance at different distance ranges on SemanticPOSS with different baselines.

Table 2: Evaluation results on the SemanticPOSS dataset with RandLA-Net as baseline.

	person	rider	car	trunk	plants	traffic sign	pole	building	fence	bike	road	mIoU
Range From 0 m to 10 m	74.3	63.8	62.5	46.1	75.0	21.6	44.2	61.9	78.1	46.5	92.1	60.6
	68.4	56.7	92.5	50.9	80.0	32.5	27.4	77.0	75.3	50.3	93.3	64.0
Improvement	-5.9	-7.1	30.0	4.8	5.0	10.9	-16.8	15.1	-2.8	3.8	1.2	3.4
Range From 10 m to 20 m	72.2	62.5	62.3	33.7	78.8	24.5	40.6	70.5	54.8	57.3	85.9	58.5
	65.6	54.5	65.7	38.0	82.2	33.8	34.0	78.1	52.2	61.9	87.8	59.4
Improvement	-6.6	-8.0	3.4	4.3	3.4	9.3	-6.6	7.6	-2.6	4.6	1.9	0.9
Range From 20 m to 30 m	64.3	54.6	47.8	30.8	73.0	24.2	39.2	81.8	33.3	47.3	72.2	51.7
	63.7	52.9	56.1	33.0	77.3	31.5	40.3	84.5	41.5	50.9	80.4	55.6
Improvement	-0.6	-1.7	8.3	2.2	4.3	7.3	1.1	2.7	8.2	3.6	8.2	3.9
Range From 30 m to 40 m	38.7	35.3	41.2	23.3	69.7	26.4	41.9	81.1	19.0	32.7	65.6	43.2
	40.7	36.3	55.7	24.6	75.4	29.0	54.8	83.6	26.2	35.9	74.2	48.8
Improvement	2.0	1.0	14.5	1.3	5.7	2.6	12.9	2.5	7.2	3.2	8.6	5.6
Range From 40 m to 50 m	20.5	16.8	28.0	19.9	63.9	19.0	25.0	76.1	11.9	25.5	59.8	33.3
	25.2	18.0	36.1	17.1	72.2	21.8	41.8	80.3	17.3	32.2	67.2	39.0
Improvement	4.7	1.2	8.1	-2.8	8.3	2.8	16.8	4.2	5.4	6.7	7.4	5.7
Range From 50 m to 60 m	17.6	2.7	23.1	10.4	61.3	17.2	19.8	78.7	7.6	17.6	47.5	27.6
	22.1	1.4	36.8	13.5	69.7	18.1	36.6	83.3	11.2	24.3	52.8	33.6
Improvement	4.5	-1.3	13.7	3.1	8.4	0.9	16.8	4.6	3.6	6.7	5.3	6.0
Range From 60 m to 70 m	13.6	0.3	5.6	6.0	65.0	11.9	15.5	78.3	13.5	14.9	27.5	22.9
	16.6	0.0	8.5	8.8	71.9	19.0	24.8	82.9	16.3	15.8	32.3	27.0
Improvement	3.0	-0.3	2.9	2.8	6.9	7.1	9.3	4.6	2.8	0.9	4.8	4.1
Range From 70 m to 80 m	8.2	0.0	2.0	5.4	58.1	3.3	13.4	79.0	4.4	7.4	21.8	18.5
	15.3	0.0	4.2	4.1	70.5	12.4	23.9	84.6	11.5	6.3	22.2	23.2
Improvement	7.1	0.0	2.2	-1.3	12.4	9.1	10.5	5.6	7.1	-1.1	0.4	4.7
Range Above 80 m	2.0	0.0	0.4	4.9	35.9	0.6	4.8	63.6	1.7	5.6	18.0	12.5
	4.9	0.0	0.5	3.2	47.5	0.7	15.8	74.9	3.5	3.2	19.4	15.8
Improvement	2.9	0.0	0.1	-1.7	11.6	0.1	11.0	11.3	1.8	-2.4	1.4	3.3
Total Range	56.8	58.2	48.1	37.8	73.4	22.3	35.4	76.6	45.4	45.7	80.9	52.8
	57.7	52.4	61.4	42.0	78.1	31.8	33.0	81.6	51.5	51.2	84.3	56.8
Improvement	0.9	-5.8	13.3	4.2	4.7	9.5	-2.4	5.0	6.1	5.5	3.4	4.0

Table 3: Evaluation results on the SemanticPOSS dataset with BAAF as baseline.

	person	rider	car	trunk	plants	traffic sign	pole	building	fence	bike	road	mIoU
Range From 0 m to 10 m	73.0	55.2	66.3	52.3	79.3	30.5	43.1	75.1	79.7	53.3	90.6	63.5
	70.0	58.6	88.5	52.6	81.4	34.6	30.5	60.9	79.9	54.9	92.9	64.1
Improvement	-3.0	3.4	22.2	0.3	2.1	4.1	-12.6	-14.2	0.2	1.6	2.3	0.6
Range From 10 m to 20 m	68.6	58.1	61.9	40.5	80.6	27.3	33.8	76.6	58.1	59.7	86.1	59.2
	69.6	63.6	66.1	36.2	81.7	24.6	36.3	75.4	63.7	62.6	87.8	60.7
Improvement	1.0	5.5	4.2	-4.3	1.1	-2.7	2.5	-1.2	5.6	2.9	1.7	1.5
Range From 20 m to 30 m	64.8	54.6	55.3	35.4	76.5	26.0	39.7	84.6	39.8	49.8	79.2	55.1
	67.0	61.1	60.2	34.0	77.5	18.6	45.8	83.3	48.5	53.7	82.0	57.4
Improvement	2.2	6.5	4.9	-1.4	1.0	-7.4	6.1	-1.3	8.7	3.9	2.8	2.3
Range From 30 m to 40 m	45.1	39.6	48.1	25.8	73.5	25.1	40.8	82.6	23.7	34.0	75.7	46.7
	43.4	43.7	57.7	24.8	75.9	27.1	49.3	83.5	31.0	38.3	76.6	50.1
Improvement	-1.7	4.1	9.6	-1.0	2.4	2.0	8.5	0.9	7.3	4.3	0.9	3.4
Range From 40 m to 50 m	22.8	24.1	31.2	16.5	65.9	11.7	23.7	76.1	15.3	24.0	70.8	34.7
	21.7	24.7	39.5	14.1	70.6	21.1	34.1	78.8	21.6	31.1	69.9	38.8
Improvement	-1.1	0.6	8.3	-2.4	4.7	9.4	10.4	2.7	6.3	7.1	-0.9	4.1
Range From 50 m to 60 m	19.9	10.0	24.2	13.5	60.6	10.8	21.4	79.6	8.2	16.6	55.2	29.1
	18.6	6.5	20.8	8.5	65.8	21.3	26.6	81.6	13.7	24.4	55.8	31.2
Improvement	-1.3	-3.5	-3.4	-5.0	5.2	10.5	5.2	2.0	5.5	7.8	0.6	2.1
Range From 60 m to 70 m	17.6	5.2	8.0	7.6	58.2	11.8	21.9	77.9	9.3	10.4	32.2	23.6
	16.8	0.5	7.4	11.7	66.9	7.4	20.8	81.6	22.1	17.4	33.0	26.0
Improvement	-0.8	-4.7	-0.6	4.1	8.7	-4.4	-1.1	3.7	12.8	7.0	0.8	2.4
Range From 70 m to 80 m	9.5	0.1	4.9	1.7	49.4	7.1	18.7	74.8	6.7	6.4	20.6	18.2
	11.3	0.0	3.7	8.3	64.6	3.7	17.9	82.5	10.3	9.7	21.3	21.2
Improvement	1.8	-0.1	-1.2	6.6	15.2	-3.4	-0.8	7.7	3.6	3.3	0.7	3.0
Range Above 80 m	2.6	0.0	1.2	5.1	29.3	0.7	11.6	66.5	2.1	4.2	10.6	12.2
	3.7	0.0	1.8	6.4	44.6	0.2	8.8	73.3	3.9	4.7	19.2	15.1
Improvement	1.1	0.0	0.6	1.3	15.3	-0.5	-2.8	6.8	1.8	0.5	8.6	2.9
Total Range	57.5	53.1	51.7	42.4	75.7	26.7	36.5	79.5	51.4	47.4	83.4	55.0
	58.1	57.6	63.2	41.8	77.9	28.9	33.8	79.8	60.1	52.2	84.9	58.0
Improvement	0.6	4.5	11.5	-0.6	2.2	2.2	-2.7	0.3	8.7	4.8	1.5	3.0

Table 4: Evaluation results on the SemanticPOSS dataset with BAF-LAC as baseline.

	person	rider	car	trunk	plants	traffic sign	pole	building	fence	bike	road	mIoU
Range From 0 m to 10 m	66.7	49.0	78.8	54.1	73.7	26.1	32.5	12.5	68.6	51.3	91.2	54.9
	66.9	63.0	89.3	54.2	78.1	33.5	55.1	2.9	78.9	58.1	92.2	61.1
Improvement	0.2	14.0	10.5	0.1	4.4	7.4	22.6	-9.6	10.3	6.8	1.0	6.2
Range From 10 m to 20 m	66.9	54.1	64.9	34.3	77.6	21.7	28.8	64.2	48.3	59.5	86.7	55.2
	68.0	58.0	62.8	42.6	75.7	32.0	39.0	59.0	54.1	61.1	86.5	58.1
Improvement	1.1	3.9	-2.1	8.3	-1.9	10.3	10.2	-5.2	5.8	1.6	-0.2	2.9
Range From 20 m to 30 m	59.7	54.4	52.9	32.3	72.7	14.9	38.7	81.5	31.0	50.5	73.1	51.0
	59.0	55.8	47.7	35.8	73.3	32.0	41.6	79.0	41.4	49.7	80.6	54.2
Improvement	-0.7	1.4	-5.2	3.5	0.6	17.1	2.9	-2.5	10.4	-0.8	7.5	3.2
Range From 30 m to 40 m	35.0	34.7	46.4	27.1	69.2	19.2	43.9	80.8	16.6	33.1	62.3	42.6
	36.5	43.7	36.3	27.5	73.2	28.9	41.3	80.4	24.8	35.0	76.2	45.8
Improvement	1.5	9.0	-10.1	0.4	4.0	9.7	-2.6	-0.4	8.2	1.9	13.9	3.2
Range From 40 m to 50 m	16.8	20.4	35.2	14.4	63.4	17.6	23.6	76.9	12.9	26.2	57.4	33.2
	20.1	34.7	22.5	19.2	70.1	24.0	27.8	78.7	16.6	29.2	71.0	37.6
Improvement	3.3	14.3	-12.7	4.8	6.7	6.4	4.2	1.8	3.7	3.0	13.6	4.4
Range From 50 m to 60 m	14.1	1.2	23.7	5.7	61.8	25.5	17.8	81.1	8.0	20.4	44.4	27.6
	20.7	7.1	19.6	12.3	67.7	31.9	30.1	82.2	12.0	24.5	57.2	33.2
Improvement	6.6	5.9	-4.1	6.6	5.9	6.4	12.3	1.1	4.0	4.1	12.8	5.6
Range From 60 m to 70 m	14.1	0.3	10.6	4.0	61.6	17.3	14.5	79.6	8.3	16.9	23.5	22.8
	18.1	0.2	6.5	6.3	68.5	27.0	22.5	81.1	13.2	17.1	34.5	26.8
Improvement	4.0	-0.1	-4.1	2.3	6.9	9.7	8.0	1.5	4.9	0.2	11.0	4.0
Range From 70 m to 80 m	9.9	0.0	3.7	3.5	55.6	9.6	11.6	79.7	6.6	8.3	16.6	18.7
	16.4	0.0	3.3	5.6	64.6	26.6	20.9	80.9	6.3	8.2	22.5	23.2
Improvement	6.5	0.0	-0.4	2.1	9.0	17.0	9.3	1.2	-0.3	-0.1	5.9	4.5
Range Above 80 m	3.7	0.0	0.8	4.5	34.6	3.4	4.8	70.1	3.5	4.4	10.6	12.8
	6.2	0.0	0.1	3.4	41.2	3.5	11.1	72.0	0.1	2.6	21.5	14.7
Improvement	2.5	0.0	-0.7	-1.1	6.6	0.1	6.3	1.9	-3.4	-1.8	10.9	1.9
Total Range	50.4	48.7	54.4	40.0	72.5	22.4	28.1	74.5	42.0	48.8	81.0	51.2
	56.4	57.7	53.8	43.5	73.9	32.1	43.3	72.5	52.8	51.4	83.8	56.5
Improvement	6.0	9.0	-0.6	3.5	1.4	9.7	15.2	-2.0	10.8	2.6	2.8	5.3

References

Hu, Q.; Yang, B.; Xie, L.; Rosa, S.; Guo, Y.; Wang, Z.; Trigoni, N.; and Markham, A. 2020. Randla-net: Efficient semantic segmentation of large-scale point clouds. In *CVPR*, 11108–11117. [1](#), [4](#)

Qiu, S.; Anwar, S.; and Barnes, N. 2021. Semantic segmentation for real point cloud scenes via bilateral augmentation and adaptive fusion. In *CVPR*, 1757–1767. [1](#), [4](#)

Shuai, H.; Xu, X.; and Liu, Q. 2021. Backward Attentive Fusing Network With Local Aggregation Classifier for 3D Point Cloud Semantic Segmentation. *IEEE Transactions on Image Processing*, 30: 4973–4984. [1](#), [4](#)